

# Battery cycler to generate open li-ion cell aging data and models

Matthias Luh, Thomas Blank

Institute for Data Processing and Electronics (IPE), Karlsruhe Institute of Technology (KIT)

Hermann-von-Helmholtz-Platz 1

76344 Eggenstein-Leopoldshafen, Germany

Tel.: +49 / (0) 721 608-29167

E-Mail: [Matthias.Luh@kit.edu](mailto:Matthias.Luh@kit.edu), [Thomas.Blank@kit.edu](mailto:Thomas.Blank@kit.edu)

URL: <https://www.ipe.kit.edu/english/>

## Acknowledgements

This work is funded by the German Research Foundation (DFG) as part of the Research Training Group 2153 “Energy Status Data – Informatics Methods for its Collection, Analysis and Exploitation”. We thank Dr. Fabian Jeschull and his colleagues from the Institute for Applied Materials (IAM) at KIT for performing the comparative electrochemical impedance spectroscopy and interpreting its results.

## Keywords

Batteries, Lifetime, Power cycling, Battery impedance measurement, Gallium Nitride (GaN)

## Abstract

Battery degradation is relevant for the lifetime, cost, and life cycle analysis of electric vehicles and stationary storages. Publicly available, reusable battery aging data is scarce and aging experiments are time-consuming and expensive. This paper starts with an overview of existing battery aging data and models. We then present our battery cycler hardware, which we intend to use to generate open battery degradation data and models. After analyzing the switching behavior, efficiency, and control behavior of the hardware, this paper gives an overview of the generated data and the user interface of the battery cycler. Finally, we provide an outlook on the further development of the project.

## Introduction

Batteries play an increasingly important role in the CO<sub>2</sub> reduction targets introduced to mitigate climate change: They are used in electric vehicles (BEV, HEV, FCEV) and stationary storage systems (home, industrial, and large-scale grid energy storage systems). Battery aging is an important aspect to consider when developing or using cells, battery systems, and applications that utilize these batteries, regardless of the cell chemistry (e.g., different kinds of lithium, sodium or lead-acid cells). The degradation of battery cells limits lifetime and, therefore, the overall cost of the application. It also affects the environmental balance and the carbon footprint of the product using the battery.

However, battery degradation is complex and dependent on many aspects. The aging of a lithium-ion cell (which is probably the most important and widespread cell type at present and in the near future) can be further differentiated into calendar aging and cyclic aging. Cycling aging occurs when the cell is charged or discharged (i.e., cycled). It is dependent on the depth of discharge (or, more specifically, the maximum and minimum voltage or State of Charge (SoC) when charging and discharging the cell), the temperature of the cell, the charging / discharging rate (i.e., the current), and the number of cycles. Calendar aging occurs at all times, even when the cell is not used, and is therefore dependent on time, but also the temperature and the voltage/SoC at which the cell is idling [1], [2]. A review of the different electrochemical aging mechanisms can be found in [3] and [4].

Modeling cell aging by considering each electrochemical effect (e.g., the temperature-dependent electrolyte decomposition) might help improve cell chemistries. However, it is too complex and afflicted with many unknown factors for product designers that select a battery cell for their application, analyze the impact of different modes of operation on the selected battery cell, or run an aging model in the

product's battery management system (BMS). Instead, heuristic mathematical models can be used for these purposes. However, cell manufacturers usually provide little information on cell aging and the influence of the parameters mentioned before. To acquire such models, an (accelerated) aging measurement of cells cycling or resting under different operating conditions can be performed. The resulting data set can then be used to fit mathematical models (e.g., the "NREL" [5] or more sophisticated models [6]) or use artificial intelligence to generate a cell aging model. However, this process is both time-consuming and very expensive because not only many cells but also cell cycler equipment with many channels are required for the cell aging measurements and deep expertise in cell aging is beneficial. Large EV manufacturers or suppliers have the means and also a substantial financial interest to run those experiments (for example, to define the battery warranty conditions). However, these companies are not interested in publishing these measurement results or only publish results that are not sufficient to derive a reusable cell model [7]. The publications with the best insight into aging results that we found are:

- A comparison of a 240 mAh "LiNi<sub>0.5</sub>Mn<sub>0.3</sub>Co<sub>0.2</sub>O<sub>2</sub> / artificial graphite (NMC532/AG)" pouch cell ("million-mile" battery) [8] with a commercial, cylindrical 2.05 Ah Sanyo UR18650E cell (previously published in [9])
- A comprehensive aging experiment using commercial, cylindrical Sanyo UR18650W cells with 1.5 Ah capacity and a "LiNi<sub>1/3</sub>Co<sub>1/3</sub>Mn<sub>1/3</sub> + LiMn<sub>2</sub>O<sub>4</sub> composite cathode" [6], [10] as well as a similar study from the same research group using commercial, cylindrical A123 26650 LiFePO<sub>4</sub> cells with 2.2 Ah capacity [11]

While the authors provide impressive results and include many graphs showing the capacity fade of the cells under different operating conditions, no raw data of the measurements are available. It is not well possible and subject to many uncertainties to use the graphs and information given in the paper to deduce a cell aging model that can be used in other investigations, e.g., to determine the capacity fade of an EV battery under different operating conditions in simulations. Due to an absence of comprehensive, public, reusable battery degradation data and models, very simple aging models are often used in research and small and medium enterprises when analyzing the aging of cells in applications. For example, some scientific authors that analyze the influence of electric vehicle charging or Vehicle-to-Grid (V2G) assume that there is a constant number of charging and discharging cycles and, optionally, a maximum lifespan of the battery in years [12]. Others assign linear and quadratic terms to energy- and power-related battery aging costs [13]. Therefore, depending on the battery model and aging assumptions used, statements about the economic viability of V2G range from "the potential profit [...] was outweighed by the cost of battery degradation" [14] to "no increased" or even "decreased aging" due to V2G [15]. Uncertainty regarding battery degradation may even prevent applications like Vehicle-to-Grid from becoming widespread and gaining acceptance, despite its enormous potential macroeconomic benefit.

We aim to produce a comprehensive cell aging dataset and model that is accessible to the public and can be reused in other investigations. For this purpose, we would like to select a representative cell that is comparable in its cell chemistry and electrical properties to cells typically used in electric cars. Part of these cells shall be exposed predominantly to cyclic aging, the other only to calendar aging. Additional cells could be exposed to cycles typical for the application, e.g., WLTP driving profiles or representative V2G patterns. The cells shall age under different parameters. For cyclically aged cells, the temperature ( $T_{cyc}$ ) as well as the current rate ( $C_{cyc\pm}$ ) and voltage limits for charging/discharging ( $V_{chg/dischg}$ ) shall be varied. For calendar-aged cells, the temperature ( $T_{cal}$ ) and the voltage ( $V_{cal}$ ) at which the cell rests shall be varied. For reasons of redundancy and a better statistical significance, even when using cells of the same batch, it is recommended to age several cells ( $N_{red}$ ) at the same parameter set. Using a relatively small set of parameters, the total number of cells quickly becomes very large, e.g., for  $T_{cyc}=T_{cal}=4$ ,  $C_{cyc\pm}=4$ ,  $V_{chg/dischg}=3$ ,  $V_{cal}=4$ ,  $N_{red}=3$ , the total number of cells is:

$$N = N_{red} \cdot (T_{cyc} \cdot C_{cyc\pm} \cdot V_{chg/dischg} + T_{cal} \cdot V_{cal}) = 192 \quad (1)$$

As commercial cyclers for a large number of cells quickly become very expensive, we aim to develop our own battery cycler hardware. A prototype of this hardware and the first results we gathered while

developing the system are presented in this paper. The battery degradation data collected with the hardware will be subject to another publication after the aging measurements ran long enough to draw robust conclusions about aging.

## Experimental setup

We developed a battery cycler prototype (shown in Fig. 1) that can charge and discharge four individual battery cells with up to 4.5 V and 7.5 A, control their temperature using different pools with a liquid cooling/heating fluid, capture the cell voltages, currents, and temperatures, and store the acquired measurement data in an easily accessible, reusable format both locally and online. In the final setup, we plan to split up the functions of the board (cycling & measurement, temperature control) into separate boards and allow each cycler board to control up to 12 cells, which is more practical and cost-effective.

The block diagram in Fig. 2 gives a schematic overview of the testbench. The prototype board, including the cycling and measurement hardware (“slave board”), is shown on the left side. It is controlled by an Infineon Aurix TriCore TC375 processor with software we developed using the TASKING TriCore Software Development Toolset.

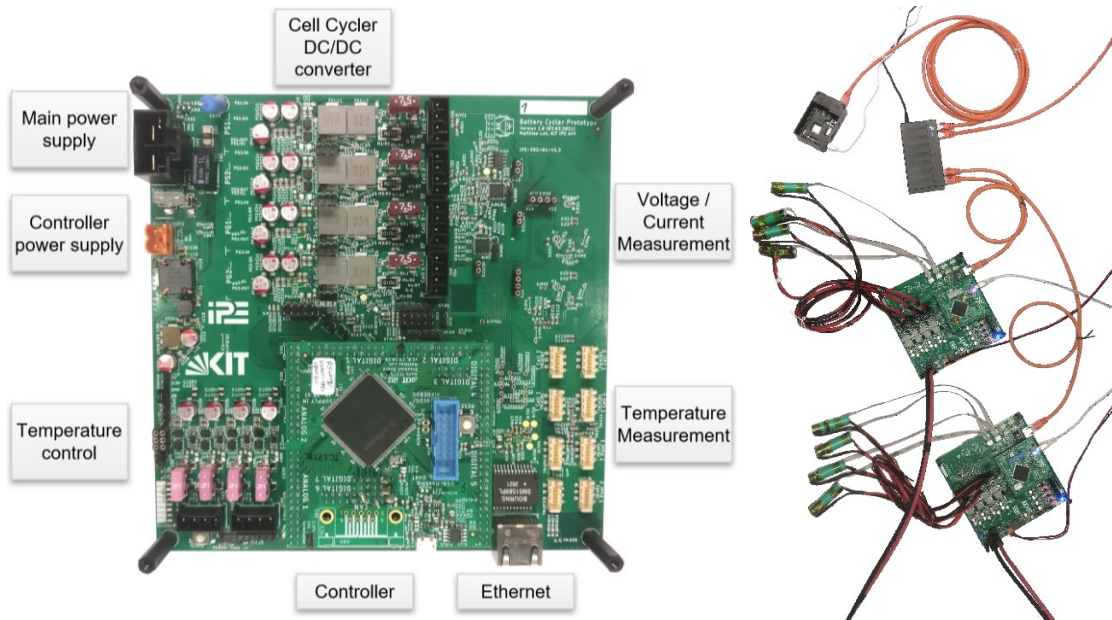


Fig. 1: Battery Cell Cycler Prototype Board (left) and exemplary setup with two cycler boards (right)

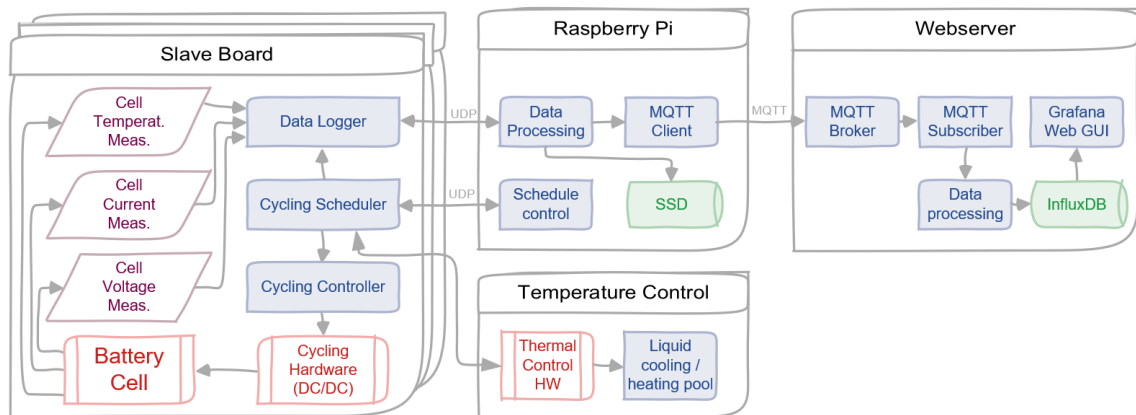


Fig. 2: Cycler testbench hardware/software components and communication structure

For each cell, an individual non-isolated DC/DC converter comprising a half-bridge is used, which adjusts the common input voltage to the voltage required to charge and discharge the cell. Gallium nitride (GaN) and silicon (Si) MOSFETs (EPC2045 from EPC Co. and RQ3E100BN from Rohm) are compared

on the prototype board to examine the most suitable type for the final board. A two-stage LC-LC filter filters the output of the DC/DC converter to obtain a smooth cell voltage and current. Fig. 3 shows a simplified schematic of the converter.

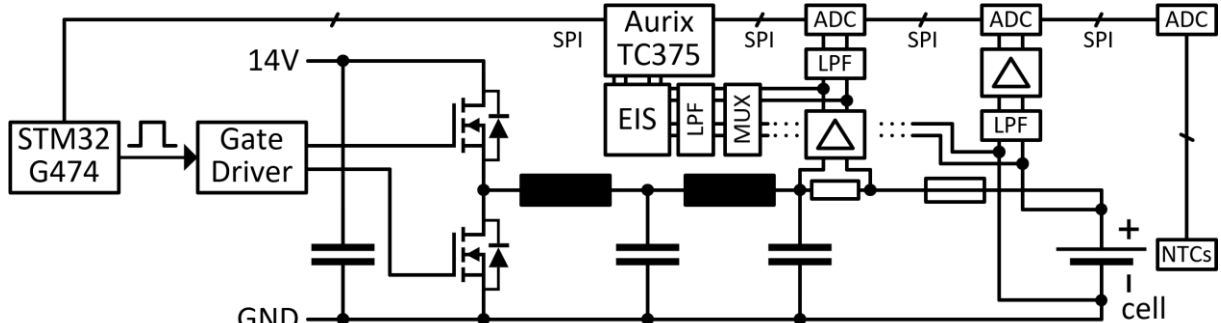


Fig. 3: Simplified schematic of the DC/DC converter with two-stage LC-filter and cell measurements

While the Aurix processor is very powerful for processing and communication, its minimum PWM timer resolution is only 10 ns. Using a switching frequency of 500 kHz, this corresponds to a 0.5 % duty cycle resolution. If an input voltage of 14 V is selected for the DC/DC converter, the open circuit output voltage could be adjusted approximately in 70 mV steps, which is too coarse for the battery cycler. Instead, the gate drivers are controlled by the high-resolution timer module (HRTIM) of an additional STM32G474 controller. The HRTIM can generate up to 12 PWM signals with a duty cycle resolution of 183.8 ps or 0.00919 %, resulting in converter output steps of approximately 0.13 mV. Using two processors per board makes the design more expensive but also safer since both processors must allow the converter to operate and each can stop cycling in case of an error or a timeout.

The cell voltages are acquired with a resolution of ca. 69  $\mu$ V in a range from 0 to 4.5 V using a differential voltage measurement circuit. A four-point measurement for separate power flow and voltage measurement contacts with four individual cables and tabs welded to the two poles of the cylindrical cells is used. A shunt and a current-sense amplifier with fast overcurrent detection are used to measure a cell current of up to  $\pm 11.25$  A with a resolution of ca. 343  $\mu$ A. Shunts with higher resistances can be used to increase accuracy in case lower cell currents are sufficient for cell cycling. There are two temperature measurement circuits per cell using NTCs connected to the casing as well as the negative pole contact of the cylindrical cells.

While the cycling controller handles the combined constant current and voltage (CC/CV) control, the cycling scheduler is responsible for the higher-level schedule. It determines when the cells are cycled, initiates check-ups in which the remaining capacity and aged impedance of the cells are measured every few days to weeks, issues a shutdown due to faults, and, if possible, handles an automatic restart.

A data logger module captures every relevant measurement and state every two seconds, stores the data on an SD card on the cycler board, and sends this data set to a Raspberry Pi via Ethernet. Multiple slave boards are connected to a Raspberry Pi. In the final setup, independent slave and Raspberry Pi boards shall be used to perform redundant measurements of similar parameter sets. On the Raspberry, the data set is stored on a local SSD and forwarded to a web server via MQTT. The web server unpacks the MQTT message and stores the individual measurements into an InfluxDB database. A Grafana web interface can be conveniently used to access the database and visualize real-time or previous measurements in a web browser remotely using customizable dashboards.

We included an option to measure the complex, frequency-dependent cell impedance using electrochemical impedance spectroscopy (EIS). Instead of an analog circuit that discharges the cell with a small sinusoidal current, the STM controller outputs a PWM pattern that excites the cell with a sinusoidal current using the DC/DC converter. Analog multiplexers connect the low-pass filtered current and differential voltage measurement signals of one cell at a time to the EIS unit. The amplitude and phase characteristics of the voltage and current measurement low-pass filters are matched to the same -3 dB cut-off frequency of approximately 33 kHz to reduce their effect on the EIS measurement while still significantly damping switching noise. Op-amps are used to hold the maximum / minimum voltage and current values and amplify their difference for an ADC. Schmitt triggers allow the processor to measure their phase angle to calculate the complex impedance.

## Preliminary results

The battery degradation measurements have not started yet and will be performed on a successor board. We plan to publish the collected raw data along with post-processed measurements and a deduced aging model of the observed cell after the cells aged on the final testbench for at least  $\frac{1}{2}$  to 1 year and conclusions about aging behavior can be drawn. Nevertheless, in this publication, we will present first measurement results using the prototype board, including measurements of the DC/DC converter switching and filtering behavior comparing GaN and Si MOSFETs, the behavior of the CC/CV controller, and the electrochemical impedance spectroscopy.

### Switching Behavior

Fig. 4 shows the switching behavior and output signals of the DC/DC converter used for cycling (charging/discharging) the cell. In the example, the cell is discharged with 5 A and has a terminal voltage of approximately 3.5 V. Three configurations of the half-bridge are compared: One using RQ3E100BN silicon MOSFETs (left column), one with EPC2045 GaN MOSFETs using the same gate resistor values (center column) and a half-bridge using the same GaN MOSFETs but with optimized gate resistor values and a snubber circuit at the output of the half-bridge (2.7 nF, 2.2  $\Omega$ ).

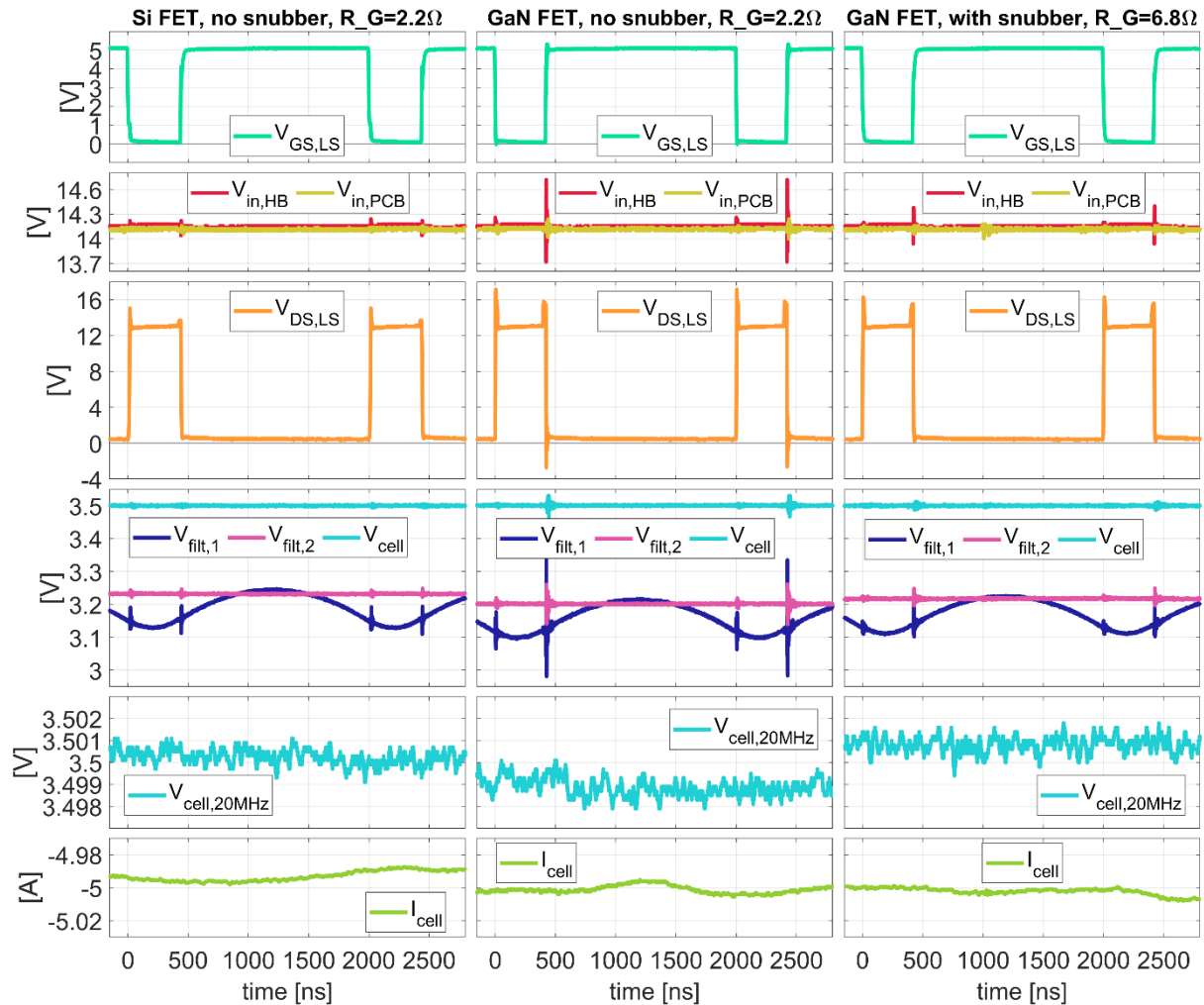


Fig. 4: Switching behavior and output signals of the cell cycling DC/DC converter

The signals were captured with a Tektronix MSO58 oscilloscope with Tektronix TPP0500B voltage probes and a Pico Technology TA018 current probe. The upper row shows the gate-source voltage of the low-side FET (turquoise), followed by the DC link voltage right in front of the examined half-bridge

(red) and at the input of the battery cycler PCB (yellow), the drain-source voltage of the low-side FET (orange), the voltage at the output of the DC/DC filter behind the first LC filter (dark blue) as well as behind the second LC filter (pink) and right at the battery cell (cyan). The bottom row shows the battery cell current (green). The battery cell voltage signal is additionally recorded in a 20 MHz bandwidth-limited measurement. The comparison of the two cell voltage signals shows that most of the noise lies in the frequency range above 20 MHz.

The switching behavior is compared in more detail in Fig. 5. It can be seen in both figures that the drain-source voltage  $V_{DS}$  is significantly overswinging when turning off and on the GaN MOSFET, while the Si MOSFET only generates relatively small ringing. The oscillations are damped by the LC filters but still influence the battery cell voltage. A higher gate resistor value ( $R_{G,ext} = 6.8 \Omega$  instead of  $2.2 \Omega$ ) was chosen for the GaN half-bridge to limit the drain-source voltage slew rates, as can be seen in Fig. 5 and Table 1. While the higher gate resistance and snubber in the gallium nitride half-bridge reduced oscillations, the silicon half-bridge still produced a less noisy cell voltage, especially during turn-on operations. In addition, the reverse voltage drop across the body diode of the silicon FET is smaller, which results in lower conduction losses during switching transitions.

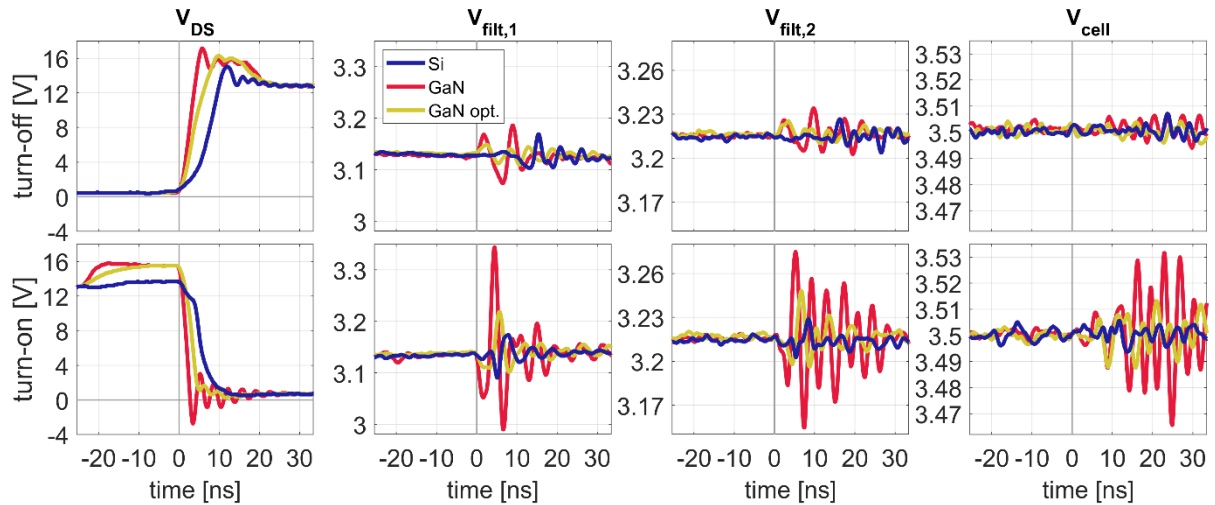


Fig. 5: Detailed comparison of switching behavior and output signals for turn-off (top row) and turn-on (bottom row) of the low-side silicon MOSFET with  $R_G = 2.2 \Omega$  (dark blue), the GaN MOSFET with  $R_G = 2.2 \Omega$  without snubber (red) and the GaN MOSFET with  $R_G = 6.8 \Omega$  and with snubber (yellow)

**Table 1:  $V_{DS}$  slew rates of the low-side MOSFET in different half-bridge configurations**

Half-bridge configuration:	Si, no snubber		GaN, no snubber		GaN, with snubber	
	$R_G = 2.2 \Omega$	$R_G = 2.2 \Omega$	$R_G = 6.8 \Omega$	$R_G = 2.2 \Omega$	$R_G = 6.8 \Omega$	
turn-off	+1.9 V/ns	+3.8 V/ns	+3.5 V/ns	+3.0 V/ns	+2.6 V/ns	
turn-on	-4.0 V/ns	-6.9 V/ns	-5.8 V/ns	-6.5 V/ns	-4.8 V/ns	

## Efficiency

The DC/DC converter was optimized for a dynamic, highly accurate low-noise operation at moderate efficiency. A comparison of the efficiencies of different half-bridge configurations at various output voltages for an output current of +3 A (charging) and -5 A (discharging) is shown in Fig. 6. The efficiency was measured by a Hioki PW3390 power analyzer using high accuracy Hioki CT6862-05 current sensors using a range of 15 V and 5 A. The voltages were measured at the input power supply plug and the cell output plug, so all losses on the PCB (including converter, filters, current measurement shunts, fuses, relay, PCB traces, and plugs) are included, but the cell and power supply cable losses are not.

As is typical for a buck converter, the efficiency at constant input voltage (here: 14 V) decreases with decreasing output voltage and increasing output current. The efficiency is about 1.5 % higher when no snubber is used. The efficiencies of Si and GaN FETs without snubber are relatively similar even though the typical  $R_{DS,ON}$  datasheet value of the silicon FET (11.0 mΩ) is about twice as high as the one of the GaN FET (5.6 mΩ). However, conduction losses in the converter are dominated by the filter and the cell fuse (ca. 35 mΩ).

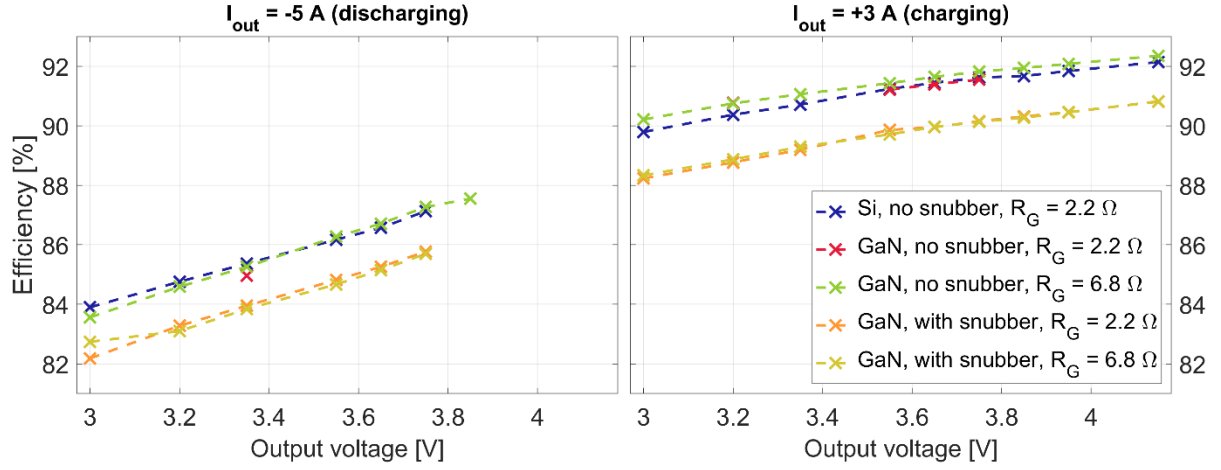


Fig. 6: Efficiency comparison of different half-bridge topologies at  $V_{in} = 14$  V

## Controller performance

The CC/CV controller is capable of a seamless transition from constant current to constant voltage. It considers the input voltage, the estimated open-circuit voltage of the cells, the cell resistance measured in the last check-up, and a fixed combined resistance for cables, PCB, filter, and MOSFETs to reach the desired output current quickly. The control algorithm runs on the Aurix processor with a frequency of 10 kHz for each cell. It calculates the desired PWM duty cycle and sends it to the STM controller via SPI. A running counter value and a CRC8 are used to detect faults in the transmission. The STM controller applies the duty cycle to the PWM running at a frequency of 500 kHz as soon as it receives and decodes the message. One PWM signal per cell is sent to an On Semi NCP81151B synchronous buck gate driver, which is connected to the two MOSFETs of the half-bridge. The PWM signals for the cells are shifted in phase to minimize the overall input current and voltage ripple.

Turn-on and turn-off procedures with an initial cell voltage of 3.5 V and a setpoint of 3.7 V / 3.0 A (charging) as well as an initial cell voltage of 3.7 V and a setpoint of 3.5 V / -5.0 A (discharging) are shown in Fig. 7. The controller reaches the desired output current after 1-3.5 ms for the first time and stabilizes the current after approximately 4-5 ms. Between 100 and 200 ms after turn-on, the current ripple measured with the oscilloscope settles down to less than  $\pm 67$  mA, the voltage ripple after the first LC-filter to  $\pm 70$  mV, and the ripple after the second cell to less than  $\pm 3$  mV (including measurement noise). In steady-state, the 20 MHz bandwidth limited signal of the cell voltage has a ripple of less than  $\pm 1$  mV and the cell current noise is below  $\pm 15$  mA. The voltage and current signals used for data acquisition and control, as well as for the EIS circuit, are low-pass filtered to further reduce switching-induced ripple and other noise.

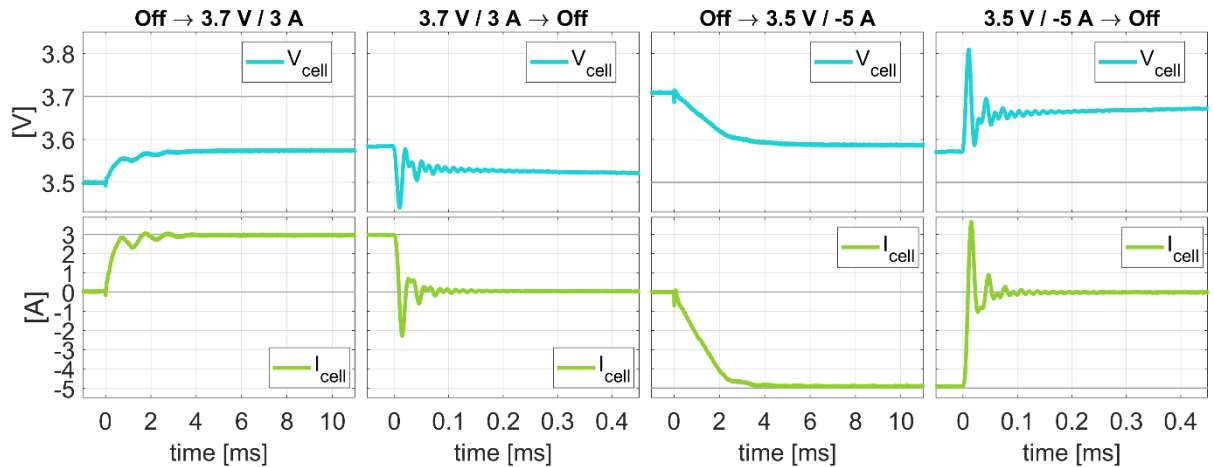


Fig. 7: Cell voltage (cyan) and current (green) when turning on the controller with a charging current of 3 A (leftmost column) and when turning off afterwards (second column) as well as when turning on with a discharging current of -5 A (third column) and turning off afterwards (rightmost column)

In Fig. 8, the same controller parameters were applied as before, but the battery cell voltage before turn-on is closer to the desired voltage limit. Hence, the controller operates in CV mode. The cell voltage limit is not violated, but the controller needs approximately 10-20 ms to reach the voltage setpoint.

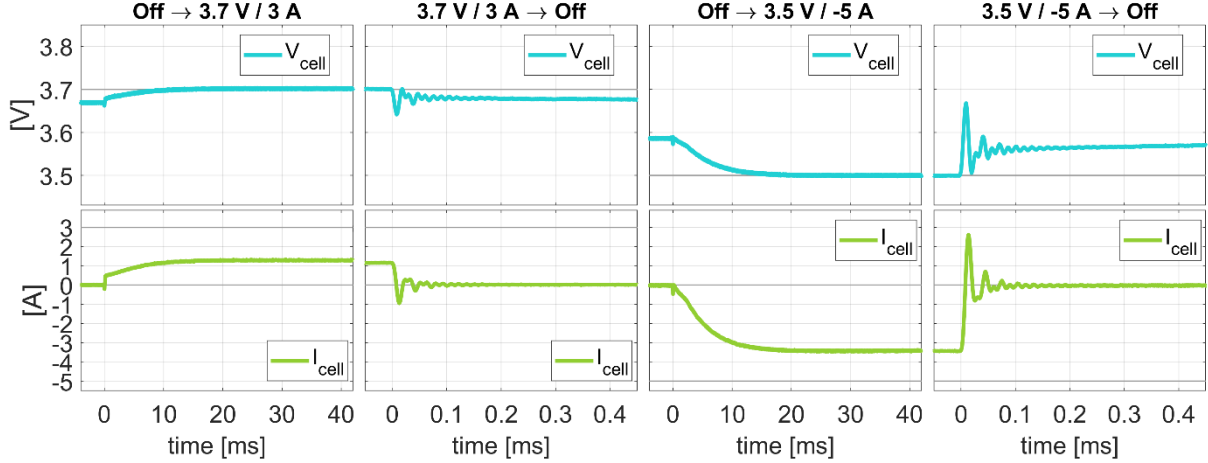


Fig. 8: Same signals and controller settings as in Fig. 7, but this time the controller runs into the current limit and smoothly transitions into constant voltage (CV) mode

## Accuracy

We compared the cycler's voltage and current measurements with commercial high-accuracy devices for a few exemplary measurement points. A more comprehensive range of accuracy measurements across the whole temperature, voltage, and current range and all cell channels was not performed.

When the battery cycler was inactive, one indicated cell voltage from the cycler was 3.4231 V, while we measured 3.4246 V with a Keithley 2470 source meter in the off state, a deviation of 1.5 mV or 0.044 %. In two other instances, the cell voltage was overestimated by 0.6 mV and 1.2 mV or 0.017 % and 0.033 %, respectively. When the cycler was discharging a cell with a set current of -5 A, the cycler indicated an average output current of -5.0000 A, while the Hioki PW3390 power analyzer using CT6862-05 current sensors measured -4.9952 A, a deviation of 4.8 mA or 0.096 %. When charging with a set current of +3 A, the cycler indicated an average current of +3.0000 A, while the power analyzer measured +2.9988 A, a deviation of 1.2 mA or 0.04 %.

## Electrochemical Impedance Spectroscopy

We performed an Electrochemical Impedance Spectroscopy (EIS) for an LG INR18650HG2 cell with our battery cycler and a commercial BioLogic VSP at different temperatures (2°C, 12°C, 22°C, 37°C) and open-circuit voltages (3.5, 3.8 V). The resulting impedance curves are shown in Fig. 9. In general, the curves match relatively well, indicating that the EIS functionality implemented on the cycler works.

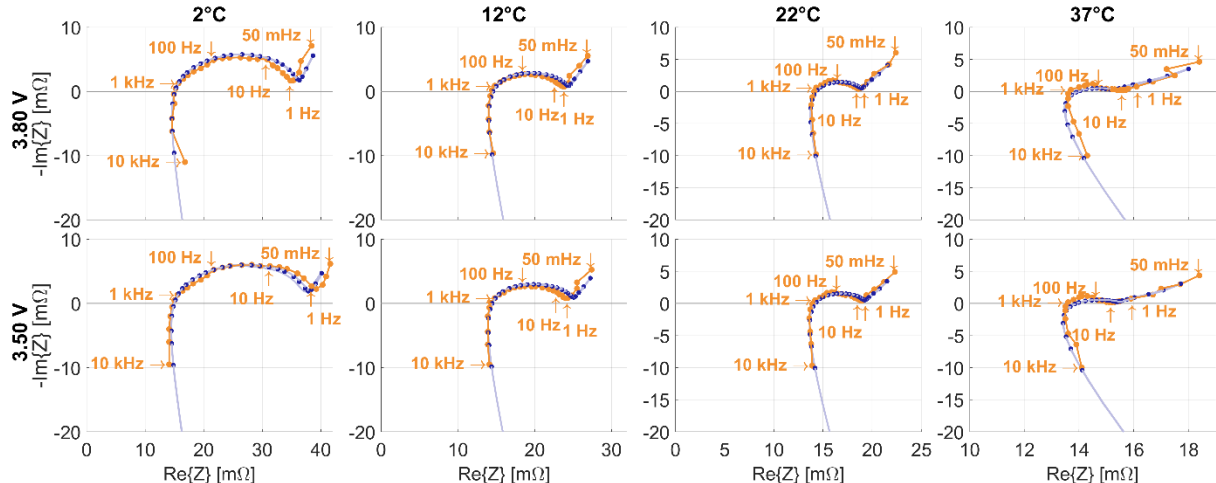


Fig. 9: EIS comparison using our battery cycler (orange) and a commercial BioLogic VSP (blue)

However, significant deviations occurred at high and very low frequencies (above 5 kHz and below 200 mHz). The average absolute amplitude error for all data points in the figure is 1.54 %, with a standard deviation of 1.46 % and a maximum error of +13.17%. The average absolute phase error is 1.03°, with a standard deviation of 0.95° and a maximum error of 4.30°.

Although the EIS results suggest the cycler is unsuitable for high-precision measurements, it is conceivable to use it for qualitative analyses, e.g., to observe the change in impedance over the cell's life.

## Data acquisition and visualization

As described before, collected data can be visualized online using the open-source tool Grafana. The data is ready to be displayed approximately 2 seconds after being collected. An example dashboard showing data of a single cell captured with the prototype is shown in Fig. 10: In the left column, the cell current (orange), voltage (dark blue), and an estimation of the open-circuit voltage (light blue) as well as the power (red) is shown. The center column shows the cell temperature (green), the estimated state of charge (yellow), as well as the added charge (light purple) and energy (dark purple) since the charging or discharging began. Important recent measurements and states are summarized in the right column.



Fig. 10: Visualization of cell measurements in a web browser using Grafana.

Additional dashboards exist for the thermal management measurements and states as well as for the EIS and long-term battery aging results. On the latter, the charge and energy extracted and charged per cycle, as well as the coulomb and energy efficiency, are shown. In addition, the total charge and energy extracted over the life of the cell and the number of cycles can be displayed.

## Conclusion

Battery aging is a critical aspect when estimating lifetime and cost or conducting a life cycle analysis of EVs and stationary storage systems. A lack of freely available, easily reusable cell aging data and models imposes many challenges and uncertainties when investigating these technologies and their use cases. Published cell aging measurements that are to some extent suitable for generating a specific cell aging model were summarized at the beginning of this paper.

We presented the prototype of a new battery cycler that we intend to use to cost-effectively perform comprehensive cell degradation experiments on li-ion battery cells to publish aging data and models that can be reused in other studies and for product development.

We compared the switching performance and efficiency of GaN and Si MOSFETs for the DC/DC converter to charge and discharge the cells. The silicon FETs cause fewer oscillations in the output voltage

and are slightly more efficient and easier to handle in our application than the BGA GaN FETs. Therefore, we prefer the Si MOSFETs for our final design. We presented the performance of the CC/CV controller, which is capable of dynamically and accurately controlling the cell current and voltage within less than 20 ms. Afterwards, we give an insight into the electrochemical impedance spectroscopy that we have implemented on the cycler and show that it matches relatively well with that of a commercial device. Finally, we presented the online data visualization tool which can be used to monitor all cells.

## Outlook

While the prototype was used to analyze different hardware and software components of the cycler, we are currently developing a more practical, cost-optimized version that can reliably and efficiently cycle more cells fully automated. Last but not least, we still have to carry out the actual experiment in which cells will be operated over a period of several months to years and analyze the measurements to generate models for degradation, which can be used in calculations and simulations. Once a model for a specific cell is derived, evaluating it with realistic profiles of different applications is desirable. It is also conceivable to analyze if the model can easily be adjusted to cells with other capacities, form factors, or chemistries using a much smaller set of reference measurements combined with the original model.

## References

- [1] Xu B., Oudalov A., Ulbig A., et al.: Modeling of Lithium-Ion Battery Degradation for Cell Life Assessment, *IEEE Transactions on Smart Grid*, vol. 9, no. 2, pp. 1131–1140, 2018, DOI 10.1109/TSG.2016.2578950
- [2] Keil P.: Aging of Lithium-Ion Batteries in Electric Vehicles, Technische Universität München, 2017
- [3] Vetter J., Novák P., Wagner M.R., et al.: Ageing mechanisms in lithium-ion batteries, *Journal of Power Sources*, vol. 147, no. 1, pp. 269–281, 2005, DOI 10.1016/j.jpowsour.2005.01.006
- [4] Alipour M., Ziebert C., Conte F.V., et al.: A Review on Temperature-Dependent Electrochemical Properties, Aging, and Performance of Lithium-Ion Cells, *Batteries*, vol. 6, no. 3, 2020, DOI 10.3390/batteries6030035
- [5] Smith K., Warleywine M., Wood E., et al.: Comparison of Plug-In Hybrid Electric Vehicle Battery Life Across Geographies and Drive-Cycles, *SAE Technical Papers*, 2012, DOI 10.4271/2012-01-0666
- [6] Purewal J., Wang J., Graetz J., et al.: Degradation of lithium ion batteries employing graphite negatives and nickel–cobalt–manganese oxide + spinel manganese oxide positives: Part 2, chemical–mechanical degradation model, *Journal of Power Sources*, vol. 272, pp. 1154–1161, 2014, DOI 10.1016/j.jpowsour.2014.07.028
- [7] Belaid S., Mingant R., Petit M., et al.: Strategies to Extend the Lifespan of Automotive Batteries through Battery Modeling and System Simulation: The MOBICUS Project, in 2017 IEEE Vehicle Power and Propulsion Conference (VPPC), 2017, DOI 10.1109/VPPC.2017.8330949
- [8] Harlow J.E., Ma X., Li J., et al.: A Wide Range of Testing Results on an Excellent Lithium-Ion Cell Chemistry to be used as Benchmarks for New Battery Technologies, *J. Electrochem. Soc.*, vol. 166, no. 13, pp. A3031–A3044, 2019, DOI 10.1149/2.0981913jes
- [9] Ecker M., Nieto N., Käbitz S., et al.: Calendar and cycle life study of Li(NiMnCo)O<sub>2</sub>-based 18650 lithium-ion batteries, *Journal of Power Sources*, vol. 248, pp. 839–851, 2014, DOI 10.1016/j.jpowsour.2013.09.143
- [10] Wang J., Purewal J., Liu P., et al.: Degradation of lithium ion batteries employing graphite negatives and nickel–cobalt–manganese oxide + spinel manganese oxide positives: Part 1, aging mechanisms and life estimation, *Journal of Power Sources*, vol. 269, pp. 937–948, 2014, DOI 10.1016/j.jpowsour.2014.07.030
- [11] Wang J., Liu P., Hicks-Garner J., et al.: Cycle-life model for graphite-LiFePO<sub>4</sub> cells, *Journal of Power Sources*, vol. 196, no. 8, pp. 3942–3948, 2011, DOI 10.1016/j.jpowsour.2010.11.134
- [12] Lehtola T. and Zahedi A.: Cost of EV battery wear due to vehicle to grid application, in 2015 Australasian Universities Power Engineering Conference (AUPEC), 2015, DOI 10.1109/AUPEC.2015.7324824
- [13] Schuller A., Dietz B., Flath C.M., et al.: Charging Strategies for Battery Electric Vehicles: Economic Benchmark and V2G Potential, *IEEE Transactions on Power Systems*, vol. 29, no. 5, pp. 2014–2022, 2014, DOI 10.1109/TPWRS.2014.2301024
- [14] Hoke A., Brissette A., Maksimović D., et al.: Electric vehicle charge optimization including effects of lithium-ion battery degradation, in 2011 IEEE Vehicle Power and Propulsion Conference, 2011, DOI 10.1109/VPPC.2011.6043046
- [15] Rosekeit M., Lunz B., Sauer D.U., et al.: Bidirektionales Ladegerät für Elektrofahrzeuge als Energiespeicher im Smart Grid - Bi-directional Charger for Electric vehicles as Energy Storage in the Smart Grid, 2012